


High-Cooperativity Coupling of Rare-Earth Spins to a Planar Superconducting Resonator

Sihao Wang¹,[✉] Likai Yang,¹ Rufus L. Cone,² Charles W. Thiel,² and Hong X. Tang¹,^{*}

¹*Department of Electrical Engineering, Yale University, New Haven, Connecticut 06511, USA*

²*Department of Physics, Montana State University, Bozeman, Montana 59717, USA*

 (Received 26 February 2022; revised 13 June 2022; accepted 14 June 2022; published 28 July 2022)

The interfacing of a superconducting microwave resonator with rare-earth-doped crystals presents a promising hybrid quantum system for applications including spin-assisted transducers and memories. The coupling strength between the spins of the rare-earth ions and the microwave photons is characterized by the cooperativity. Here, we report an ultrahigh cooperativity of $C \sim 650$ between rare-earth spins and a planar superconducting microwave resonator that features a highly uniform magnetic field for harnessing the strong anisotropic coupling strength of erbium-doped yttrium orthosilicate. This cooperativity rivals that from a bulk dielectric resonator and may pave a path for efficient coupling of spins with microwave photons on an integrated platform.

DOI: [10.1103/PhysRevApplied.18.014071](https://doi.org/10.1103/PhysRevApplied.18.014071)

I. INTRODUCTION

Rare-earth ions (REIs) have been an attractive candidate for quantum information processing due to their favorable optical and spin properties. Their stable optical transition and high fluorescence quantum efficiency allow spin control and detection through optical photons [1,2]. Extremely long coherence times from electronic and nuclear spins make REIs an ideal choice for quantum information storage [3,4]. Furthermore, their narrow homogeneous linewidth presents opportunities for spectral multiplexing in a broader inhomogeneous linewidth of the spin ensemble [5]. Among rare-earth elements, erbium (Er) emerges as a popular choice because of its optical transitions in the telecommunication band. This avoids the need for frequency conversion and facilitates integration with existing fiber-optic technology.

Common choices of host crystals for REIs include yttrium orthosilicate (Y_2SiO_5), yttrium orthovanadate (YVO_4), and lithium niobate (LiNbO_3). Yttrium orthosilicate (YSO) gains its popularity due to its weak environmental nuclear magnetic moments. Efficient long-lived multimode photonic memories [6–8] have been demonstrated using REI-doped YSO, which enables entanglement storage [9], quantum teleportation [10], and quantum state transfer from atomic vapor [11].

Strong microwave coupling with spins is essential in enabling efficient quantum state manipulation [12], isolating a spin ensemble from the environmental spin bath [13], and relaxing the optical-coupling requirement for a

high-efficiency microwave-to-optical transducer [14]. Due to the large mode-size mismatch, and hence the poor mode overlap between resonant spins and the microwave photon field, microwave resonators are often employed to enhance their coupling strengths. These include both bulk three-dimensional (3D) cavities [15–19] and planar superconducting resonators [20–25]. By providing a homogeneous magnetic field (B field) and high spatial mode overlap with the embedded REI-doped crystal, 3D dielectric cavities benefit from spin-number enhancement from the REI ensemble and enable an ultrahigh cooperativity of $C \sim 600$ [19]. On the other hand, planar superconducting resonators offer a small device footprint and mode volume and thus enhanced single-spin coupling rates. However, the magnetic field distribution tends to become less uniform with microscale patterned structures, thus reducing the effective modal overlap between spins and the rf magnetic field. Experiments on coupling to rare-earth ions have so far yielded a cooperativity of $C \sim 30$ [23,25]. Further improvement is required to improve the mode overlap while maintaining a high Q factor.

In this work, we present an ultrahigh cooperativity of $C \sim 650$ between Er^{3+} ions and a niobium nitride (NbN) superconducting microwave resonator through designing the parallel nanowire strips for a homogeneous B field and utilizing the anisotropic coupling strength in an erbium-doped yttrium orthosilicate (Er:YSO) crystal. We use flip-chip bonding techniques to integrate the Er:YSO crystal on a NbN superconducting resonator with a Q factor of $Q > 10^5$. Electron-spin resonance (ESR) spectra are measured at different orientations to demonstrate strong coupling and high cooperativity.

^{*}hong.tang@yale.edu

II. MEASUREMENT

A commercial bulk 10-ppm-natural-abundance Er:YSO crystal (Scientific Materials) is cut into a cuboid ($5\text{ mm} \times 4\text{ mm} \times 3\text{ mm}$) along the three dielectric axes (D_1 , D_2 , and b) and flip-chip bonded on a NbN superconducting microwave resonator, with the b axis perpendicular to the bonding interface. The thin film of 50-nm NbN is grown on a high-resistivity silicon substrate using atomic layer deposition (ALD), with a sheet resistance of $R_{\text{sq}} \sim 45\ \Omega/\text{sq}$. We fabricate microwave resonators by patterning hydrogen silsequioxane (HSQ) on NbN thin film with electron-beam lithography (EBL) and etching in reactive-ion etching (RIE) with chlorine. The resonator has the shape of a racetrack for strong coupling with the hoop antenna. The width, radius, and straight-section length of the racetrack resonator are $100\ \mu\text{m}$, $800\ \mu\text{m}$, and $1500\ \mu\text{m}$, respectively. Three parallel $1\text{-}\mu\text{m}$ -wide strips act as inductors that replace one straight section of the racetrack resonator. These inductor strips are connected to the racetrack resonator through interdigitated (IDT) capacitors. This design allows the generated vortices inside the racetrack resonator to traverse out, hence stabilizing the cavity frequency under a strong external B field. The final flip-chip-bonded device is housed in a copper-cavity box to reduce radiation loss to the environment. Figure 1(a) shows a photograph of the device inside the copper box. The external static B field B_0 is applied parallel to the inductor strips. The oscillating B field B_1 from the inductor strips is therefore perpendicular to B_0 . The use of flip-chip bonding permits free orientation of the Er:YSO crystal on the microwave resonator. Figure 1(b) is an optical micrograph of the NbN microwave resonator. The narrow inductor strips are magnified in the inset. The corresponding circuit model is shown in Fig. 1(c), where the microwave resonator is modeled as an LC resonator and the hoop antenna as an inductor. Figure 1(d) is the cross-section plot of the oscillating B field B_1 from the inductor strips. As opposed to the commonly used meander inductors where the current in the adjacent straight sections flows in opposite directions, the current in the three parallel-inductor strips flows in the same direction, resulting in a more uniform B field B_1 inside the bonded Er:YSO crystal. Figure 1(e) is the oscillating B field B_1 strength at $35\ \mu\text{m}$ above the NbN microwave resonator, indicated by the dashed line in Fig. 1(d). A homogeneous B field distribution above the inductor strips plays an important role in reducing the spin linewidth.

The packaged device is loaded in the mixing chamber of a dilution fridge with a base temperature of 10 mK. The actual device temperature is 30 mK due to a thermal gradient. A vector network analyzer (VNA) is used to measure the S_{21} response. The microwave resonator has a resonance frequency of 5.7 GHz at zero applied B field $B_0 = 0$. The Q factor of the cavity is fitted with a Fano resonance to

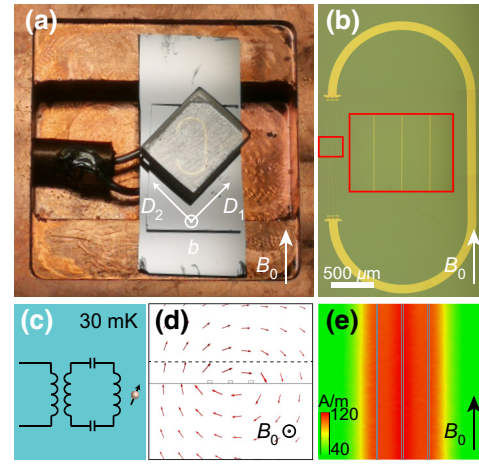


FIG. 1. (a) A photograph of the packaged device. The NbN microwave resonator is fabricated on a high-resistivity silicon substrate that sits on a larger piece of high-resistivity silicon carrier in a copper cavity. A hoop antenna is used to couple to the device. The crystal axes are indicated and the applied static magnetic field B_0 is oriented parallel to the resonator inductor strips. (b) An optical micrograph of the NbN resonator. An enlarged image of the narrow inductor strips is shown in the inset. (c) The corresponding circuit model of the device. (d) The cross-section arrow plot of the oscillating magnetic field B_1 around the inductor strips. The thin strips are exaggerated for viewing purposes. (e) The oscillating magnetic field profile at $35\ \mu\text{m}$ above the microwave resonator, indicated by the dashed line in (d). The uniform magnetic field facilitates a narrow spin linewidth. The narrow inductor strips are exaggerated for illustration purposes.

take the background response into account. $Q \sim 130\ 000$ is obtained at the input power of $-70\ \text{dBm}$, at which the loss from two level systems is minimized.

The Hamiltonian of the coupled system is given as

$$H = \mu_B \mathbf{B} \cdot \mathbf{g} \cdot \mathbf{S} - \mu_n g_n \mathbf{B} \cdot \mathbf{I} + \mathbf{I} \cdot \mathbf{Q} \cdot \mathbf{I} + \mathbf{S} \cdot \mathbf{A} \cdot \mathbf{I}, \quad (1)$$

where μ_B (μ_n) is the electron (nuclear) Bohr magneton, $g_n = -0.1618$ is the nuclear g factor, \mathbf{g} is the anisotropic electron g -factor tensor, \mathbf{Q} is the nuclear quadrupole tensor, and \mathbf{A} is the hyperfine interaction tensor. The first two terms of the spin Hamiltonian are the electron and nuclear Zeeman splittings, which are proportional to the applied B field B_0 . The third and the fourth terms are the nuclear quadrupole interaction and the hyperfine interaction, which are independent of B_0 . Based on the published tensor values [26,27], we can calculate the eigenenergy spectra of the Er:YSO crystal at different orientations [28].

The crystal structure of Er:YSO is described by space group C_{2h}^6 , where Er^{3+} ions substitute Y^{3+} ions at two distinct crystallographic sites, both characterized by C_1 symmetry. For each crystallographic site, the C_2 rotation symmetry and inversion symmetry of the crystal give rise

to four subclass sites in the crystal with different local orientations. Based on their response to the applied B field, these subclass sites can be further divided into two groups. The group related to the inversion symmetry is magnetically equivalent, as it responds identically to a B field of arbitrary direction. The other group related to the C_2 symmetry is magnetically inequivalent. These two subclass sites interact with an applied B field differently, except for two special cases, when the B field is either applied along the b axis or in the D_1 - D_2 plane. During the measurement, a static B field B_0 is applied parallel to the inductor strips in the D_1 - D_2 plane to minimize the vortex-induced loss. The oscillating B field B_1 from the inductors is perpendicular to B_0 . Figures 2(a) and 2(b) are the Breit-Rabi diagrams of Er^{3+} ions at sites 1 and 2 when the oscillating B field B_1 is approximately 20° from the D_1 axis. The strong electron-spin transitions due to the electron Zeeman term at both sites under the selection rule $\Delta m_s = \pm 1$ are marked by the red arrows. The odd-number isotope ^{167}Er has a nuclear spin of $I = 7/2$, resulting in satellite hyperfine spin-state transitions (black arrows) with $\Delta m_i = 0$ and the nuclear quadrupole transitions (blue arrows) with $\Delta m_i = \pm 1$.

The lengths of the arrows are selected to match the microwave resonance frequency, to demonstrate the positions of level anticrossing. This level anticrossing is manifested as the coupling of the microwave field to the spins and hence an additional loss channel of the resonator, resulting in a drop in the Q factor of the microwave resonance. In the case of perfect alignment, only one level anticrossing for Er^{3+} ions, and therefore one dip of the Q factor at each site, should be observed when sweeping the B field strength. However, two dips are observed (see Fig. S1 in the Supplemental Material [29]), indicating a small misalignment between the applied B field and the D_1 - D_2 plane. By utilizing an additional balance coil with an applied B field in the perpendicular direction, we are able to cancel the out-of-plane component of B_0 . The deviation angle is estimated to be approximately 1.05° , which is comparable to the expected uncertainty in the crystal orientation. Figure 2(c) shows the variation of the Q factor with the sweeping B field. The solid (dashed) markers represent the assignment of each level anticrossing to the spin-state transition at each site in Figs. 2(a) and 2(b). The prominent dips correspond to the strong Zeeman electron-spin-state transitions and the satellite dips correspond to the transitions with nuclear hyperfine states. Figure 2(d) is the corresponding frequency shift of the microwave resonance at level-anticrossing fields. The background quadratic dependence of the microwave resonance frequency on B_0 due to the nonlinearity from the kinetic inductance in the narrow inductor strips is normalized to highlight the frequency shift.

The collective coupling ν between the spin ensemble and the microwave resonator is proportional to the effective

g factor by $\nu = g\mu_B\sqrt{n\xi\omega_0\mu_0/(4\hbar)}$, where μ_B is the Bohr magneton, $n \sim 10^{17} \text{ cm}^{-3}$ is the concentration of Er^{3+} ions, $\xi \sim 0.25$ is the geometry factor accounting for the mode overlap with spins and the spin coupling with the oscillating field, and ω_0 is the microwave resonance frequency. For an oscillating B field B_1 in the D_1 - D_2 plane, the collective coupling strength is maximized when the angle between B_1 and the D_1 axis is close to 120° and minimized when the angle is near 30° . Figure 3(a) shows the evolution of the microwave resonance with the sweeping B field B_0 when B_1 is at an angle of 20° to the crystal axis D_1 for Er^{3+} ions at site 1. The level anticrossing near $B_0 = 48 \text{ mT}$ can be extracted. The modified resonator frequency ω and decay rate κ are fitted with a simplified phenomenological

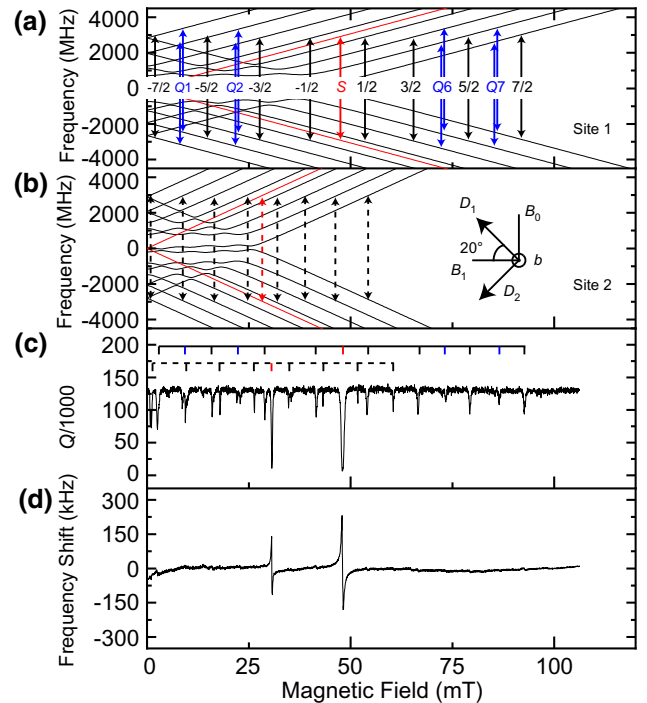


FIG. 2. (a) The simulated Breit-Rabi diagram of $\text{Er}:\text{YSO}$ for spins residing at site 1 subject to an oscillating magnetic field B_1 oriented 20° from the D_1 axis in the D_1 - D_2 plane. The allowed and forbidden transitions at 5.7 GHz are shown by solid arrows with different colors. (b) The corresponding Breit-Rabi diagram for spins at site 2. The allowed transitions are shown by dashed arrows with different colors. The inset shows a schematic of the orientation of the YSO crystal with respect to the magnetic fields. (c) The spectrum of the loaded Q factor of the superconducting microwave resonator with the static magnetic field B_0 . Each dip in the spectrum indicates a level anticrossing between the spin and microwave modes. Transitions from site 1 (2) are indicated with solid (dashed) markers. (d) The frequency shift of the ESR spectrum with the static magnetic field B_0 . The quadratic dependence of the superconducting microwave resonance with the static magnetic field B_0 is normalized.

model [21,25]:

$$\omega = \omega_0 - \frac{v^2 \Delta}{\Delta^2 + \gamma_s^2/4}, \quad (2)$$

$$\kappa = \kappa_c + \frac{v^2 \gamma_s}{\Delta^2 + \gamma_s^2/4}, \quad (3)$$

where $\Delta = \omega - \omega_0$ is the detuning, γ_s is the spin inhomogeneous linewidth, and κ_c is the initial microwave-cavity decay rate. Figures 3(b) and 3(c) show the fitting of the frequency shift and linewidth, yielding the collective coupling strength $v = (2\pi)2.5$ MHz, the spin-ensemble inhomogeneous linewidth $\gamma_s = (2\pi)26.6$ MHz, and the cavity linewidth $\kappa_c = (2\pi)41$ kHz. The cooperativity is thus $C = 4v^2/(\kappa_c \gamma_s) = 22$.

For a large cooperativity, we rotate the Er:YSO crystal so that the angle between B_1 and the D_1 axis is 112° , near 120° for maximum g . Figure 3(d) is a similar plot of the resonance evolution with sweeping B_0 when B_1 is at 112° to the crystal axis D_1 for Er^{3+} ions at site 1. At this orientation, the coupling of the spins to the oscillating B field B_1 is maximized but the interaction with the static B field B_0 is minimized. The out-of-plane component of B_0 is beyond the compensation range of the balance coil. Therefore, no balance coil is applied at 112° and the applied B_0 deviates by approximately 1.05° from the D_1 - D_2 plane. This deviation results in the lifting of the degeneracy of the subclass sites related to the C_2 rotation of the crystal lattice.

The resonator frequency and decay rate are fitted with a modified model to account for the double level anticrossings from the subclass levels:

$$\omega = \omega_0 - \frac{v_1^2 \Delta}{\Delta^2 + \gamma_1^2/4} - \frac{v_2^2 \Delta}{\Delta^2 + \gamma_2^2/4}, \quad (4)$$

$$\kappa = \kappa_c + \frac{v_1^2 \gamma_1}{\Delta^2 + \gamma_1^2/4} + \frac{v_2^2 \gamma_2}{\Delta^2 + \gamma_2^2/4}, \quad (5)$$

where $v_{1(2)}$ and $\gamma_{1(2)}$ are the collective coupling strength and the linewidth for ions at subclass level 1 (2), respectively. Figures 3(e) and 3(f) show the fitting of the frequency shift and the linewidth, yielding $v_1 = (2\pi)12.5$ MHz, $v_2 = (2\pi)12.2$ MHz, $\gamma_1 = (2\pi)18.5$ MHz, $\gamma_2 = (2\pi)18.1$ MHz, and $\kappa_c = (2\pi)51$ kHz. The corresponding cooperativities for each subclass are $C_1 = 4v_1^2/(\kappa_c \gamma_1) = 650$ and $C_2 = 4v_2^2/(\kappa_c \gamma_2) = 634$.

The cooperativity of $C \sim 650$ is one order of magnitude larger than the literature values from cases with planar superconducting microwave resonators, rivaling that from the 3D cavity with high spin-number enhancement. Yet, this cooperativity can be further optimized. Our current manual alignment during the flip-chip bonding process is not perfect, causing the crystal orientation to deviate from the optimal angle for the g factor. The lifting of

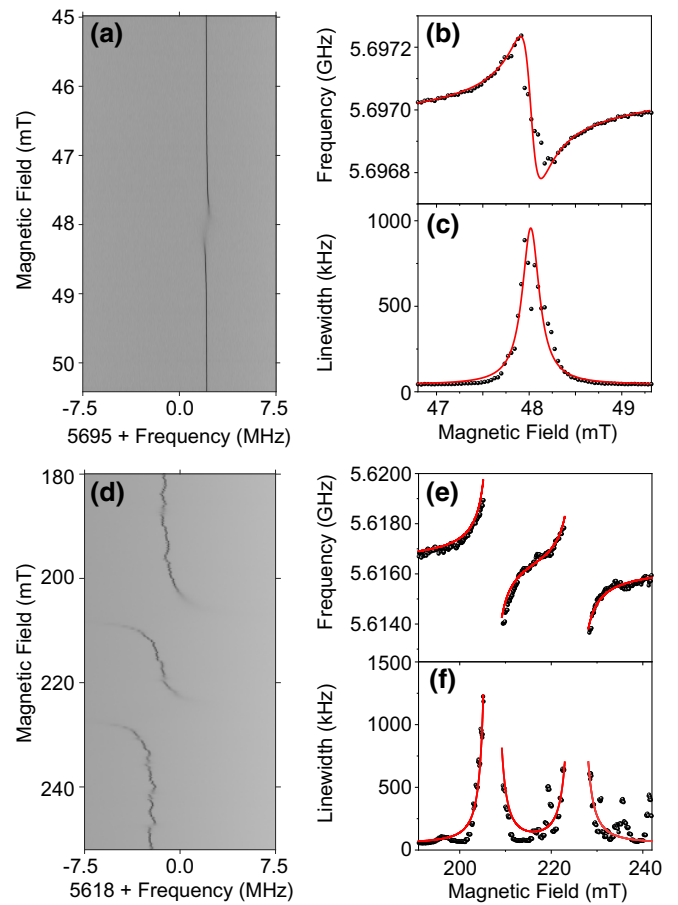


FIG. 3. (a)–(c) The electron-spin level anticrossing for the oscillating magnetic field B_1 oriented 20° from the D_1 axis in the D_1 - D_2 plane. (a) The S_{21} spectra of the microwave resonance when sweeping the static magnetic field B_0 across the level-anticrossing point. (b) The frequency shift as a function of the applied static magnetic field B_0 and the fitting. (c) The resonator linewidth as a function of the applied static magnetic field B_0 and the fitting. (d)–(f) The electron-spin level anticrossing for the oscillating magnetic field B_1 oriented 112° from the D_1 axis. The two subclass modes indicate that the magnetic field is slightly off from the D_1 - D_2 plane. (d) The S_{21} spectra of the microwave resonance when sweeping the static magnetic field B_0 across the level-anticrossing point. (e) The frequency shift as a function of the applied static magnetic field B_0 and the fitting. (f) The resonator linewidth as a function of the applied static magnetic field B_0 and the fitting.

degeneracy due to the out-of-plane B field can be suppressed with a larger balance coil, bringing about a twofold improvement as spins from both subclasses contribute. Further improvement could come from the reduction of vortex-induced microwave loss and hence a smaller κ_c . These improvements are evidenced by the fitting results from the double level anticrossings without a balance coil at 20° (see Fig. S1 in the Supplemental Material [29]). Fitting with Eqs. (4) and (5) yields $v_1(20^\circ) = (2\pi)1.5$ MHz, $v_2(20^\circ) = (2\pi)1.6$ MHz, $\gamma_1(20^\circ) = (2\pi)18.7$ MHz,

$\gamma_2(20^\circ) = (2\pi)18.8$ MHz, and $\kappa_c(20^\circ) = (2\pi)51$ kHz. The corresponding cooperativities are $C_1(20^\circ) = 9$ and $C_2(20^\circ) = 11$. Note that the spin linewidth γ_s is higher when the balance coil is applied. This is likely due to the imperfect cancellation of the out-of-plane B field, so that the two level anticrossings do not overlap completely. The flip-chip bonding process may still leave a small gap between the crystal and the superconducting resonator, reducing the geometry overlapping factor ξ . The theoretical estimation of the coupling strength with zero gap and $g = 12$ at $\xi \sim 0.25$ is $\nu_{\text{theo}} \sim (2\pi)28.7$ MHz, which is more than twice as high as the current extracted value, resulting in a cooperativity of thousands. The direct deposition and fabrication of superconducting resonators on the Er:YSO crystal [25] is a potential solution for minimizing the gap but at the expense of the flexibility to orientate the crystal at an arbitrary angle.

III. CONCLUSION

In conclusion, we realize high-cooperativity coupling between an Er^{3+} spin ensemble and a microwave resonator by producing a more homogeneous B field and exploiting the anisotropic g -factor tensor. An ultrahigh cooperativity of $C = 650$ is achievable, which is comparable to that from large 3D resonators with high spin-number enhancement. This result marks a step toward a high-efficiency microwave-to-optical transducer, an essential component in building a coherent link between a superconducting quantum circuit and optical quantum network. The strong coupling also paves the way for spin manipulation and detection, such as cooling of spin ensembles and high-sensitivity spin detection. An efficient state transfer and mapping in and out of the spin states with strong coupling is highly desirable in a quantum memory device.

ACKNOWLEDGMENTS

This work is supported by the Department of Energy, Office of Basic Energy Sciences, Division of Materials Sciences and Engineering under Grant No. DE-SC0019406. We would like to thank Dr. Yong Sun, Sean Rinehart, Kelly Woods, and Dr. Michael Rooks for the assistance provided in the device fabrication. The fabrication of the devices was done at the Yale School of Engineering & Applied Science (SEAS) Cleanroom and the Yale Institute for Nanoscience and Quantum Engineering (YINQE).

[1] T. Zhong, J. M. Kindem, J. G. Bartholomew, J. Rochman, I. Craiciu, E. Miyazono, M. Bettinelli, E. Cavalli, V. Verma, S. W. Nam, *et al.*, Nanophotonic rare-earth quantum memory with optically controlled retrieval, *Science* **357**, 1392 (2017).

[2] S. Chen, M. Raha, C. M. Phenicie, S. Ourari, and J. D. Thompson, Parallel single-shot measurement and coherent control of solid-state spins below the diffraction limit, *Science* **370**, 592 (2020).

[3] M. Zhong, M. P. Hedges, R. L. Ahlefeldt, J. G. Bartholomew, S. E. Beavan, S. M. Wittig, J. J. Longdell, and M. J. Sellars, Optically addressable nuclear spins in a solid with a six-hour coherence time, *Nature* **517**, 177 (2015).

[4] Y. Ma, Y.-Z. Ma, Z.-Q. Zhou, C.-F. Li, and G.-C. Guo, One-hour coherent optical storage in an atomic frequency comb memory, *Nat. Commun.* **12**, 1 (2021).

[5] W. R. Babbitt, Z. W. Barber, S. H. Bekker, M. D. Chase, C. Harrington, K. D. Merkel, R. K. Mohan, T. Sharpe, C. R. Stiffler, A. S. Traxinger, *et al.*, From spectral holeburning memory to spatial-spectral microwave signal processing, *Laser Phys.* **24**, 094002 (2014).

[6] M. P. Hedges, J. J. Longdell, Y. Li, and M. J. Sellars, Efficient quantum memory for light, *Nature* **465**, 1052 (2010).

[7] M. Sabooni, Q. Li, S. Kröll, and L. Rippe, Efficient Quantum Memory Using a Weakly Absorbing Sample, *Phys. Rev. Lett.* **110**, 133604 (2013).

[8] C. Laplane, P. Jobez, J. Etesse, N. Gisin, and M. Afzelius, Multimode and Long-Lived Quantum Correlations between Photons and Spins in a Crystal, *Phys. Rev. Lett.* **118**, 210501 (2017).

[9] C. Clausen, I. Usmani, F. Bussières, N. Sangouard, M. Afzelius, H. de Riedmatten, and N. Gisin, Quantum storage of photonic entanglement in a crystal, *Nature* **469**, 508 (2011).

[10] F. Bussières, C. Clausen, A. Tiranov, B. Korzh, V. B. Verma, S. W. Nam, F. Marsili, A. Ferrier, P. Goldner, H. Herrmann, *et al.*, Quantum teleportation from a telecom-wavelength photon to a solid-state quantum memory, *Nat. Photonics* **8**, 775 (2014).

[11] N. Maring, P. Farrera, K. Kutluer, M. Mazzera, G. Heinze, and H. de Riedmatten, Photonic quantum state transfer between a cold atomic gas and a crystal, *Nature* **551**, 485 (2017).

[12] A. Bienfait, J. Pla, Y. Kubo, X. Zhou, M. Stern, C. Lo, C. Weis, T. Schenkel, D. Vion, D. Esteve, *et al.*, Controlling spin relaxation with a cavity, *Nature* **531**, 74 (2016).

[13] B. Albanese, S. Probst, V. Ranjan, C. W. Zollitsch, M. Pechal, A. Wallraff, J. J. Morton, D. Vion, D. Esteve, E. Flurin, *et al.*, Radiative cooling of a spin ensemble, *Nat. Phys.* **16**, 751 (2020).

[14] L. A. Williamson, Y.-H. Chen, and J. J. Longdell, Magneto-Optic Modulator with Unit Quantum Efficiency, *Phys. Rev. Lett.* **113**, 203601 (2014).

[15] S. Probst, A. Tkalčec, H. Rotzinger, D. Rieger, J.-M. Le Floch, M. Goryachev, M. Tobar, A. Ustinov, and P. Bushev, Three-dimensional cavity quantum electrodynamics with a rare-earth spin ensemble, *Phys. Rev. B* **90**, 100404 (2014).

[16] X. Fernandez-Gonzalvo, Y.-H. Chen, C. Yin, S. Rogge, and J. J. Longdell, Coherent frequency up-conversion of microwaves to the optical telecommunications band in an Er:YSO crystal, *Phys. Rev. A* **92**, 062313 (2015).

[17] Y.-H. Chen, X. Fernandez-Gonzalvo, S. P. Horvath, J. V. Rakonjac, and J. J. Longdell, Hyperfine interactions of

- Er³⁺ ions in Y₂SiO₅: Electron paramagnetic resonance in a tunable microwave cavity, *Phys. Rev. B* **97**, 024419 (2018).
- [18] D. L. Creedon, K. Benmessaï, W. P. Bowen, and M. E. Tobar, Four-Wave Mixing from Fe³⁺ Spins in Sapphire, *Phys. Rev. Lett.* **108**, 093902 (2012).
- [19] W. G. Farr, M. Goryachev, J.-M. Le Floch, P. Bushev, and M. E. Tobar, Evidence of dilute ferromagnetism in rare-earth doped yttrium aluminium garnet, *Appl. Phys. Lett.* **107**, 122401 (2015).
- [20] I. Wisby, S. De Graaf, R. Gwilliam, A. Adamyan, S. Kubatkin, P. Meeson, A. Y. Tzalenchuk, and T. Lindström, Angle-Dependent Microresonator ESR Characterization of Locally Doped Gd³⁺:Al₂O₃, *Phys. Rev. Appl.* **6**, 024021 (2016).
- [21] P. Bushev, A. Feofanov, H. Rotzinger, I. Protopopov, J. Cole, C. Wilson, G. Fischer, A. Lukashenko, and A. Ustinov, Ultralow-power spectroscopy of a rare-earth spin ensemble using a superconducting resonator, *Phys. Rev. B* **84**, 060501 (2011).
- [22] M. U. Staudt, I.-C. Hoi, P. Krantz, M. Sandberg, M. Simoen, P. Bushev, N. Sangouard, M. Afzelius, V. S. Shumeiko, G. Johansson, *et al.*, Coupling of an erbium spin ensemble to a superconducting resonator, *J. Phys. B: At. Mol. Opt. Phys.* **45**, 124019 (2012).
- [23] S. Probst, H. Rotzinger, S. Wünsch, P. Jung, M. Jerger, M. Siegel, A. Ustinov, and P. Bushev, Anisotropic Rare-Earth Spin Ensemble Strongly Coupled to a Superconducting Resonator, *Phys. Rev. Lett.* **110**, 157001 (2013).
- [24] A. Tkalčec, S. Probst, D. Rieger, H. Rotzinger, S. Wünsch, N. Kukharchyk, A. Wieck, M. Siegel, A. Ustinov, and P. Bushev, Strong coupling of an Er³⁺-doped YAlO₃ crystal to a superconducting resonator, *Phys. Rev. B* **90**, 075112 (2014).
- [25] G. Dold, C. W. Zollitsch, J. O'sullivan, S. Welinski, A. Ferrier, P. Goldner, S. de Graaf, T. Lindström, and J. J. Morton, High-Cooperativity Coupling of a Rare-Earth Spin Ensemble to a Superconducting Resonator Using Yttrium Orthosilicate as a Substrate, *Phys. Rev. Appl.* **11**, 054082 (2019).
- [26] O. Guillot-Noël, P. Goldner, Y. Le Du, E. Baldit, P. Monnier, and K. Bencheikh, Hyperfine interaction of Er³⁺ ions in Y₂SiO₅: An electron paramagnetic resonance spectroscopy study, *Phys. Rev. B* **74**, 214409 (2006).
- [27] Y. Sun, T. Böttger, C. Thiel, and R. Cone, Magnetic *g* tensors for the ⁴*i*_{15/2} and ⁴*i*_{13/2} states of Er³⁺: Y₂SiO₅, *Phys. Rev. B* **77**, 085124 (2008).
- [28] S. Stoll and A. Schweiger, EASYSYSPIN, a comprehensive software package for spectral simulation and analysis in EPR, *J. Magn. Reson.* **178**, 42 (2006).
- [29] See the Supplemental Material at <http://link.aps.org/supplemental/10.1103/PhysRevApplied.18.014071> for the experimental data and the corresponding fittings of the double level anticrossings at 20° without a balance coil.